

Revision 2

1 Thermal conductivity of molten and glassy  $\text{NaAlSi}_3\text{O}_8$ ,  
2  $\text{CaMgSi}_2\text{O}_6$  and  $\text{Mg}_2\text{SiO}_4$  by Non Equilibrium Molecular  
3 Dynamics at elevated Temperature and Pressure: Part 1-  
4 Methods and Results

5

6

7

8

Dane Tikunoff<sup>1</sup> and Frank J. Spera<sup>1\*</sup>

9

<sup>1</sup>Department of Earth Science, University of California-Santa Barbara,

10

\*E-mail: [spera@geol.ucsb.edu](mailto:spera@geol.ucsb.edu)

11

12

13

## Revision 2

### 14 **Abstract**

15 Non Equilibrium Molecular Dynamics (NEMD) simulations are used to compute the  
16 phonon thermal conductivity ( $k$ ) for liquids and glasses of composition  $\text{Mg}_2\text{SiO}_4$ ,  
17  $\text{CaMgSi}_2\text{O}_6$  and  $\text{NaAlSi}_3\text{O}_8$  at 2000-4500 K and 0-30 GPa based on classical potentials.  
18 These compositions span the range of melt polymerization states in natural systems at  
19 ambient pressure. The NEMD results compare well with available laboratory  
20 measurements on molten  $\text{NaAlSi}_3\text{O}_8$  and  $\text{CaMgSi}_2\text{O}_6$  at 1-bar. Thermal conductivities  
21 decrease with increasing temperature ( $T$ ), increase with increasing pressure ( $P$ ) and, at  
22 low pressure, increase slightly as the mean coordination number of Si and Al around  
23 oxygen increases, in the sequence  $\text{Mg}_2\text{SiO}_4$ ,  $\text{CaMgSi}_2\text{O}_6$  and  $\text{NaAlSi}_3\text{O}_8$ . At 3500 K, the  
24 thermal conductivity of  $\text{CaMgSi}_2\text{O}_6$  at 0, 10, 20 and 30 GPa is 1.1, 2.1, 2.5 and 3 W/m K,  
25 respectively. At ambient pressure ( $0.2 \pm 0.15$  GPa),  $k=1.2$  and  $0.5$  W/m K at 2500 K and  
26 4500 K, respectively for  $\text{CaMgSi}_2\text{O}_6$ . For  $\text{NaAlSi}_3\text{O}_8$  composition,  $k$  varies from 1.7 W/m  
27 K to 2.7 W/m K at 3050 K for pressures of 6 and 30 GPa, respectively.  $\text{Mg}_2\text{SiO}_4$  liquid at  
28 ambient pressure ( $0.07 \pm 0.16$  GPa) is found to have thermal conductivities of 1.36 and  
29 0.7 W/m K at 2500 K and 4500 K, respectively. Tables giving computed  $k$  values for all  
30 compositions are included for state points studied. The trade-off between  $T$  and  $P$  implies  
31 that the phonon thermal conductivity of silicate liquids at mantle depths increases  
32 substantially (factor of 2-3) along isentropes.

33

## Revision 2

34

# INTRODUCTION

35 Knowledge of the phonon thermal conductivity of amorphous silicates (melts and  
36 glasses) over the range of composition (X), P and T of the Earth's crust and mantle is  
37 essential for analysis of many geophysical and geochemical problems. For example, heat  
38 transfer during nucleation and dissolution or growth of a crystal from a melt is a  
39 significant factor governing rock texture. Similarly, heat exchange between magma and  
40 its surroundings is relevant to rates of magma crystallization, mechanisms of volatile-  
41 saturation and the thermodynamics of partial melting. Heat transport from the Earth's  
42 core to mantle, possibly modulated by a transient molten or partially molten ultra-low  
43 velocity zone (ULVZ), is relevant to the long-term thermal history of Earth, the thickness  
44 of thermal boundary layers along the core-mantle boundary and the strength and  
45 evolution of the Earth's magnetic field (Wen and Helmberger, 1998; Hernlund and  
46 Jellinek, 2010; Idehara, 2011; Anzellini et al, 2013; Olsen, 2013). Accurate values of the  
47 thermal diffusivity,  $\kappa = k/\rho C_p$ , where  $\rho$  is the density,  $C_p$  is the isobaric specific heat  
48 capacity, and  $k$  is the phonon thermal conductivity, are needed to calculate transient  
49 geotherms and predict conditions for crustal anatexis and metamorphism in orogenic  
50 regions (e.g., Whittington et al., 2009). Finally, in ceramic and composite materials  
51 processing, knowledge of thermal conductivity is required (Kang and Morita, 2006). Of  
52 special concern is the lack of any estimates of the effects of pressure on phonon  
53 conduction in silicate liquids. In this study, attention is mainly focused upon equilibrium  
54 silicate liquids of petrological significance although a few results relevant to glasses are  
55 included. The term amorphous is used here to refer to either glass or liquid when the  
56 distinction is not essential.

## Revision 2

57           There are few reliable measurements of the thermal conductivity of molten  
58 silicates as a function of X and T at ambient P. We are aware of *no* experimental  
59 measurements describing the effect of pressure on k for silicate liquids. Although there  
60 are measurements and theory related to the effects of pressure on thermal conductivity in  
61 crystalline silicates and oxides, liquids are structurally distinct with essentially no long  
62 range structure beyond  $\sim 0.5$  nm (Kittel, 1949). Hence, one might expect some  
63 differences in modes of phonon excitation in liquids relative to ordered solids because,  
64 unlike solids, liquids undergo gradual changes in structure as P increases. One of the  
65 goals of this study is to provide quantitative constraints on the pressure-dependence of  
66 the thermal conductivity of silicate liquids at elevated temperature. Very limited  
67 experimental data at 1-bar on molten silicates of varying atomic-level structure suggest  
68 that at fixed T and P, the more polymerized the melt (e.g., the lower the NBO/T ratio),  
69 the higher the thermal conductivity (Kang and Morita, 2006). A second goal of this work  
70 is to therefore examine, at fixed temperature and pressure, the correlation of thermal  
71 conductivity with NBO/T ratio. Finally, although for crystalline solids at constant  
72 pressure, thermal conductivity varies according to  $1/T$  (e.g., see summary in Stackhouse  
73 and Stixrude, 2010) the validity of this scaling of conductivity with temperature,  $k \propto 1/T$ ,  
74 has not been experimentally or numerically studied for molten silicates in the range 2000-  
75 5000 K. The high-T scaling of k at fixed P is therefore also investigated here. In short,  
76 current knowledge of the thermal conductivity of silicate liquids is meager. In this study,  
77 we study of the effects of P, T and melt composition on the phonon thermal conductivity.  
78           Obtaining accurate values for the phonon thermal conductivity proves difficult in  
79 the laboratory (e.g., Tritt and Weston, 2004). Many measurements are of restricted value

## Revision 2

80 because: (1) they are contaminated by unwanted radiative (photon) transport, (2) include  
81 unwanted interfacial contact effects or (3) are affected by convective heat transport. For  
82 example, measurements reported by McBirney and Murase (1973) using the hot-wire  
83 method are dominated by radiative effects that act to conceal the smaller phonon  
84 contribution. Additionally, in hot-wire and hot-layer methods, thermal losses at contacts  
85 introduce significant errors difficult to eliminate without complex deconvolution (Healy  
86 et al, 1976; Lee and Hasselman, 1985, Hammerschmidt and Sabuga, 2000). Hofmeister  
87 and co-workers (Pertermann and Hofmeister, 2006; Hofmeister, 2007; Hofmeister et al,  
88 2009; Pertermann et al, 2008) present measurements of thermal conductivity at ambient  
89 pressure for a number of compounds. They note that recent advances in contact-free,  
90 laser-flash analysis and better data reduction methods (Degiovanni et al., 1994; Mehling  
91 et al., 1998) enable removal of direct radiative transfer effects and losses to the container  
92 and hence provide accurate phonon conductivities at ambient P and temperatures just  
93 above 1-bar melting points. Unfortunately, these measurements are limited to 1-bar ( $10^{-4}$   
94 GPa) pressure. Although these data indicate that k decreases weakly with increasing T in  
95 the range ~1300-1600 K for silicate liquids, the behavior at higher temperature has not  
96 been studied and there are no data on the effects of pressure. Data on alkali halides and  
97 metal liquids (e.g., Beck et al, 2007; Galamba et al, 2004; de Koker et al, 2012) suggests  
98 that conductivity increases with pressure along an isotherm but for silicate liquids the  
99 effects of pressure are unknown. Consequently, the trade-off between variations in T and  
100 P is unknown for liquid silicates. Finally, although studies on CaO-Al<sub>2</sub>O<sub>3</sub>-SiO<sub>2</sub> liquids  
101 (Kang and Morita, 2006), as well as molten diopside and molten albite (Hofmeister et al.,  
102 2009) suggest that that polymerized or strong ‘network’ liquids exhibit higher k at similar

## Revision 2

103 T and P compared to less polymerized ‘fragile’ liquids (Martinez and Angell, 2001), the  
104 role of composition and its correlative melt polymerization is not well quantified.  
105 Because melt structural states correlate with changes in second order thermodynamic  
106 property differences between liquid and glass (e.g., isothermal expansivity, isothermal  
107 compressibility, isobaric heat capacity), (Giordano and Dingwell, 2003) one might expect  
108 a correlation at fixed T and P between melt composition and phonon conductivity such  
109 that more fragile melts possess lower conductivities compared to the network (strong)  
110 melts. This conjecture can be addressed using liquid structural states, encapsulated in  
111 radial distribution analysis and coordination statistics derived from MD simulations (e.g.,  
112 Ghiorso and Spera, 2009; Spera et al, 2009). The compositions chosen in this study span  
113 the spectrum of polymerization states relevant to natural magmas (Mysen and Richet,  
114 2005; Hendersen et al, 2006; Hofmeister et al, 2009). That is, in forsterite liquid the  
115 canonical fraction of bridging oxygen at low pressure,  $X_{BO} (=N_{BO}/(N_{BO}+N_{NBO}))$ ,  
116 approaches zero whereas albite liquid is fully polymerized with each oxygen being shared  
117 between two distinct Si-Al tetrahedra (i.e.,  $X_{BO}=1$ ). Diopside liquid is intermediate in the  
118 stoichiometric sense with  $X_{BO}=1/3$  at 1-bar pressure. One of the most significant  
119 connections between structure and properties observed in all liquid silicates both  
120 experimentally and in Molecular Dynamics simulations is the increasing coordination of  
121 cations around oxygen (and of oxygen with itself) as pressure increases (e.g., Daniel et al,  
122 1996; Allwardt et al, 2007; Spera et al, 2011). This effect dominates a smaller but  
123 opposing temperature effect of lengthening bond distances. As shown below, the higher  
124 mean coordination number of metals around oxygen gives rise to an increase in the  
125 thermal conductivity as pressure increases along an isotherm for all of the compositions

## Revision 2

126 studied here. Hence along a mantle adiabat, the thermal conductivity of a melt is expected  
127 to increase with depth. At crustal pressures  $\sim 0$ -2 GPa, composition effects will dominate.  
128 An important result of this study explored more fully in part II is that at the same  
129 temperature and crustal pressure, the thermal conductivity of silicic melt (e. g., a rhyolite)  
130 is larger by 25-100 % compared to basaltic melt. In summary, the effects of composition,  
131 temperature and pressure on thermal conductivity in silicate liquids are largely unknown  
132 over the range of states relevant to the Earth. The main purpose of this study is to address  
133 these issues.

## METHODS

134  
135  
136 Classical Molecular Dynamics

137  
138 The calculations in this study are based on classical Molecular Dynamics (MD)  
139 simulations. In classical MD, an empirical relation describing the potential energy  
140 between atom pairs is used to compute forces between atoms. This pairwise additive,  
141 radially symmetric potential is derived *a priori* and is not part of the MD simulation.  
142 Based on these forces, particles are moved to new positions following the dictates of  
143 Newton's second law of motion for several million femtosecond ( $10^{-15}$  s) time steps.  
144 From the locations and velocities of the particles, various thermodynamic and transport  
145 properties are computed using the formalism of macroscopic thermodynamics and  
146 statistical mechanics. The potential of Matsui (1998) for the system Na<sub>2</sub>O-CaO-MgO-  
147 SiO<sub>2</sub>-Al<sub>2</sub>O<sub>3</sub> was utilized in this study. This potential incorporates Coulombic, Born and  
148 van der Waals energies and fractional charges on the atoms. The Matsui potential has  
149 been used in previous studies to determine the equation of state, tracer diffusivity and  
150 shear viscosity for CaAl<sub>2</sub>Si<sub>2</sub>O<sub>8</sub>, CaMgSi<sub>2</sub>O<sub>6</sub>, MgSiO<sub>3</sub>, Mg<sub>2</sub>SiO<sub>4</sub>, and 1-bar eutectic

## Revision 2

151 composition (system  $\text{CaMgSi}_2\text{O}_6$ - $\text{CaAl}_2\text{Si}_2\text{O}_8$ ) liquid (Creamer, 2012; Martin et al., 2012;  
152 Spera et al., 2011; Ghiorso and Spera, 2009; Spera et al., 2009; Nevins et al., 2009;  
153 Martin et al., 2009). The Matsui potential provides a reasonable representation of these  
154 liquids up to circa 30 GPa based on comparisons with laboratory data and results from  
155 first-principles MD simulations on similar compositions (e.g., Sun et al, 2011; Karki et al,  
156 2011; Stixrude et al, 2009). Technical details of the basic MD methodology are described  
157 in Spera et al. (2009, 2011) and follow standard MD protocols. The time step used in all  
158 simulations is 1 femtosecond (1 fs). All NEMD calculations for the thermal conductivity  
159 start from a thermally equilibrated initial state following the methods described in Spera  
160 et al. (2011).

161

### 162 Distinguishing Equilibrium Liquid from Non-equilibrium Glass

163 The pressure-temperature range of state points studied for both  $\text{NaAlSi}_3\text{O}_8$  and  
164  $\text{CaMgSi}_2\text{O}_6$  spans the transition from an equilibrium liquid to a non-equilibrium glass on  
165 the timescale of the MD simulation. The simulations for  $\text{Mg}_2\text{SiO}_4$  composition pertain  
166 wholly to the liquid. It is important to make the distinction between glass and liquid  
167 (melt) because the properties of a glass depend on its history unlike that of an equilibrium  
168 or metastable liquid (Donth, 2001). When temperature is decreased rapidly on a liquid  
169 and its intrinsic relaxation time exceeds the laboratory or simulation quenching timescale,  
170 the liquid falls out of equilibrium and undergoes a kinetic transition to a glass. The glass  
171 transition temperature ( $T_g$ ) for a given composition depends on both quench rate and  
172 pressure (Passaglia and Martin, 1964). The glass transition is not a transition in the  
173 thermodynamic sense, but instead a kinetic phenomenon, where the amorphous solid with

## Revision 2

174 crystal-like vibrational properties is dynamically arrested and hence preserves the  
175 disorder of the liquid (Roland et al, 2005; Langer, 2014). At typical laboratory cooling  
176 rates of  $\sim 0.1$ -1 K/s, the glass transition temperature ( $T_g$ ) for  $\text{NaAlSi}_3\text{O}_8$  and  $\text{CaMgSi}_2\text{O}_6$   
177 liquids are 1036 K and 1023 K, respectively, at 1 bar (Arndt and Häberle, 1973, Reinsch  
178 et al, 2008). Because the effective quench rates used in MD simulations are vastly  
179 greater, of order  $\sim 10^2$  K/ps ( $10^{14}$  K/s), the computer glass transition temperature is  
180 significantly higher. For example, the computer  $T_g$  of  $\text{CaAl}_2\text{Si}_2\text{O}_8$  defined by analysis of  
181 the mean square displacement *versus* time (see below) is approximately 2800 K for a  
182 quench rate of 70- 200 K/ps (Morgan and Spera, 2001). This is significantly higher than  
183 the laboratory value of  $T_g = 1025$  K (Arndt and Häberle, 1973).

184         The transition from liquid to glass can be detected in MD simulations by two  
185 means. For ergodic liquids an excellent correlation exists between the potential energy  
186 ( $E_{\text{POT}}$ ) and  $T^{3/5}$  at constant density (Spera et al, 2009; Ghiorso and Spera, 2009; Martin et  
187 al, 2012; Creamer, 2012). This scaling relationship, proposed by Rosenfeld and Tarazona  
188 (1998), is called RT-scaling. Glasses exhibit imperfect RT scaling; on plots of  $E_{\text{POT}}$  vs  
189  $T^{3/5}$  deviations from linearity along isochores occur around  $T_g$  and become more  
190 pronounced as T decreases. A dynamical method for detection of the glass transition is  
191 based on the mobility of atoms (tracer diffusivity) in Euclidean space. In an ergodic  
192 liquid, the mean square displacement (MSD) of an atom is a linear function of time; a  
193 plot of MSD vs. t in logarithmic coordinates exhibits a slope of unity after a short ( $< 100$   
194 fs) ballistic interval (Morgan and Spera, 2001). In contrast, glassy materials exhibit the  
195 phenomena of sub-diffusion; a **diffusion** process with a non-linear relationship to time, in  
196 contrast to a normal diffusion process in which the **mean squared displacement** (MSD) of

## Revision 2

197 a particle is a linear function of time (Wang et al, 2012). In particular, in the non-ergodic  
198 region where sub-diffusion holds, the MSD exhibits power-law behavior with  $MSD \sim t^\delta$   
199 following a short ballistic interval. The exponent  $\delta$  in a thermally arrested liquid (i.e., a  
200 glass) is characterized by  $\delta < 1$  (Metzler and Klafter, 2004; Weeks and Weitz, 2002). Sub-  
201 diffusion arises when a system possesses memory, the hallmark of a non-equilibrium  
202 material such as glass. For  $CaMgSi_2O_6$  the computer glass transition in our simulations  
203 occurs at  $\sim 2630 \pm 50$  K at 1 bar. For  $NaAlSi_3O_8$  composition,  $T_g$  is approximately 2800  
204 K based on the RT scaling and MSD criteria. The glass transition temperature depends on  
205 pressure in addition to quench rate. The variation of the computer glass transitions with  
206 pressure for  $CaMgSi_2O_6$  and  $NaAlSi_3O_8$  found here empirically lies in the range 10-30  
207 K/GPa. In the Tables below for thermal conductivity, glasses are distinguished from  
208 liquids based on the RT and MSD analysis outlined above for compositions  $NaAlSi_3O_8$   
209 and  $CaMgSi_2O_6$ . The emphasis in this study is on equilibrium ergodic liquids, although  
210 some glass results are included.

### 211 Non-Equilibrium Molecular Dynamics

212  
213 Calculations of thermal conductivity from MD simulations can be performed in  
214 two ways: Equilibrium MD (EMD) or NEMD. The Green-Kubo method, an EMD  
215 approach, uses heat current fluctuations to compute the thermal conductivity *via* the  
216 Kubo relations (Kubo, 1966). The microscopic definition of the heat flux for EMD  
217 involves interparticle dynamic correlations requiring evaluation of pair velocities and  
218 particle energies that are computationally expensive to evaluate and subject to large  
219 fluctuations (Rapaport, 1995). Convergence of the current-current correlation function  
220 can be slow. Here we employ a Non Equilibrium Molecular Dynamics (NEMD) method,

## Revision 2

221 which is relatively easy to implement, and has proved to be reliable (e.g., Müller-Plathe,  
222 1997; Müller-Plathe and Bordat, 2004). In particular, the NEMD method has been  
223 successfully applied to liquids giving excellent results in comparison with laboratory  
224 measurements (Cao, 2008; Bedrov et al., 2000; Terao et al., 2007) and Green-Kubo  
225 (EMD) calculations (Vogelsang et al., 1987).

226 The essential idea of the NEMD method used to obtain  $k$  is to impose a known  
227 heat flux on the system by exchange of particle kinetic energies and then determine the  
228 resulting steady-state temperature gradient in the direction parallel to the heat flux. The  
229 thermal conductivity can then be expressed

$$230 \quad k = \frac{\left\langle \int_0^{t_D} q_z(t) dt \right\rangle}{2At_D(dT/dz)} \quad (1)$$

231 where the integral is the cumulative heat flow imposed during a simulation of duration  $t_D$   
232 in the  $z$  direction,  $A$  is the cross-sectional area of the plane orthogonal to the  $z$ -axis, and  
233 the temperature derivative is the observed linear temperature gradient once a stationary  
234 thermal profile is achieved in the system. In order to impose a heat flux and compute the  
235 temperature profile, the simulation box is divided into  $N$  slabs perpendicular to the  $z$   
236 direction. In the present work  $N$  lies between 20-50; all layers are of identical volume.  
237 The heat flux is created by exchanging the barycentric velocities of identical type atoms  
238 (e.g., O for O, Ca for Ca, etc) between what becomes a cold layer located in the middle of  
239 the simulation box and what becomes a hot layer adjacent to one of the domain  
240 boundaries. In particular, the velocity exchange is accomplished by switching an atom  
241 with the largest kinetic energy (i.e., the hottest) from the cold slab with an atom of the  
242 same type with the lowest kinetic energy (coldest) in the hot layer. Serial application of

## Revision 2

243 this procedure induces a temperature gradient for a known quantity of heat exchange  
244 based on the kinetic energies of the exchanged atoms. The instantaneous local kinetic  
245 temperature  $\langle T_k \rangle$  in the  $k^{\text{th}}$  slab is given by

$$246 \quad T_k = \frac{1}{3k_B n_k} \sum_{i=1}^{n_k} m_i v_i^2 \quad (2)$$

247 where the sum extends over all  $n_k$  atoms of each type of mass  $m_i$  and velocity  $v_i$  in the  $k^{\text{th}}$   
248 slab. This exchange mechanism produces an energy transfer computed from

$$249 \quad \left\langle \int_0^{t_D} q_z(t) dt \right\rangle = \sum_{\text{transfers}} (v_c^2 - v_h^2) \quad (3)$$

250 The heat transfer leads to a temperature difference between the designated layers and  
251 gives rise to a steady-state temperature gradient across each half of the system. This  
252 temperature gradient is the desired quantity of the NEMD simulation. Exchanging the  
253 velocities of two atoms of equal mass (e.g., an O for an O, a Ca for a Ca, etc) leaves the  
254 total linear momentum, total kinetic energy, melt composition and the internal energy  
255 unchanged. After reaching the thermal steady state, the energy transfer imposed by the  
256 velocity exchange is exactly balanced by the heat flux in the opposite direction effected  
257 by the phonon thermal conductivity of the liquid. The thermal conductivity is then  
258 computed from the expression

$$259 \quad k = \frac{\sum_{\text{transfers}} (v_c^2 - v_h^2)}{2t_D L_x L_y (dT / dz)} \quad (4)$$

260 The sum is taken over all transfers over the duration  $t_D$  of the NEMD simulation starting  
261 from an equilibrated initial state. All quantities in Eq. (4) are known exactly except the  
262 temperature gradient that is obtained from Eq. (2) applied to each layer. The simulation is  
263 terminated after a linear or nearly linear temperature gradient is established.

## Revision 2

264 Representative thermal profiles are given in Tikunoff (2013). Attainment of a linear T  
265 profile typically requires simulations of 1-5 ns duration. In this study, tetragonal periodic  
266 primary MD ‘boxes’ with  $L_z > L_x=L_y$ , as well as cubic boxes are used. When cubic boxes  
267 are used, uncertainty in  $k$  is smaller, because more atoms are being simulated and  
268 uncertainty of state point conditions scales according to  $N_T^{-1/2}$  where  $N_T$  is the total  
269 number of atoms used in the simulation. At each state point studied, simulations are  
270 performed for several different simulation cell sizes to take account of finite-size effects  
271 (see below). Because of the mirror plane at  $z=L_z/2$ , each simulation provides  $2N$   
272 temperatures over distance  $L_z$ . The thermal gradient is determined by linear regression of  
273 these  $2N$  values each at a specific value of  $z$  corresponding to the mid-point of the layer.  
274 The uncertainty of the thermal conductivity ( $\sigma_k$ ) is found by propagation of error of the  
275 temperature gradient found by regression of  $T$  against  $z$ . The value of  $k$  computed from  
276 Eq (4) corresponds to the thermal conductivity at the mean temperature and pressure of  
277 the simulation. Typically, with systems of 8000 atoms the uncertainty in  $T$  and  $P$  are  $\pm 30$   
278 K and  $\pm 0.25$  GPa, respectively. These uncertainties can be made smaller by using more  
279 particles since  $\sigma_T$  and  $\sigma_P$  scale according to  $N^{-1/2}$ . For example, with  $N=24,000$  particles,  
280  $1\sigma$  fluctuations in  $T$  and  $P$  are  $\sigma_T \approx 18$  K and  $\sigma_P \approx 0.15$  GPa, respectively. In this study  $N_T$   
281 varied from 2500 to 350,000 and weighted regression has been used in all cases to find  
282 the best statistical fits.

283

284 Critical NEMD parameters

285       There are two critical parameters in an NEMD simulation used to compute  $k$ : the  
286 duration between particle swaps ( $\Omega$ ) or its reciprocal, the swap frequency, and the longest

## Revision 2

287 dimension of the MD rectangular domain ( $L_z$ ). Tuning of these parameters insures good  
288 precision in  $k$  and efficient use of computational resources. In order to find the trade-off,  
289 a number of simulations for molten diopside at ambient pressure and high  $T$  at various  $\Omega$   
290 and  $L_z$  were conducted. Comparison with the laboratory measurements from Hofmeister  
291 et al. (2009) at identical (within uncertainty) state points for  $\text{CaMgSi}_2\text{O}_6$  affords an  
292 objective evaluation of the quality of the NEMD simulations (see below). Additional  
293 NEMD simulations were run on crystalline and supercritical argon, a benchmark material  
294 in MD studies, in an earlier phase of this research; these results are presented elsewhere  
295 (Tikunoff, 2013) where additional technical details may be found.

### 296 *Role of swap period ( $\Omega$ )*

297         The swap period ( $\Omega$ ) is the period, in units of femtoseconds (fs), between particle  
298 velocity swaps during the NEMD calculation. The calculated conductivity of amorphous  
299  $\text{CaMgSi}_2\text{O}_6$  at ambient pressure ( $10^{-4}$  GPa) and 1700 K in a box of fixed  $L_z$  with its one-  
300 sigma error ( $\sigma_k$ ) is plotted against  $\Omega$  in Figure 1. For the limiting value of  $\Omega=1$  (not  
301 shown on Figure 1), or one swap per 1 fs time step, the system does not have sufficient  
302 time between velocity exchanges for thermal relaxation and relatively large statistical  
303 fluctuations for the thermal gradient occur that obfuscate determination of the  
304 conductivity. In contrast, for low swap periods ( $\Omega=100$  or one exchange every 100 fs)  
305 long simulation times are required for the system to achieve a steady-state temperature  
306 profile since relatively little heat is transferred per swap. In this case, for fixed simulation  
307 duration  $t_D$ , the uncertainty  $\sigma_k$  is relatively large, roughly 10-15 %, relative due to slow  
308 convergence. Values of  $\Omega$  between 20-40 give  $\sigma_k$  errors in the 2-6 % range, relative. In  
309 light of the trade-off between computational burden and desired precision, values for  $\Omega$  in

## Revision 2

310 this range appear optimal and have been used here. Similar results were found for argon  
311 fluid (Tikunoff, 2013). For  $\Omega$  in this range,  $k$  can be found with statistical uncertainty of  
312 several percent, approximately equal to or less than experimental uncertainties in  $k$  for  
313 silicate liquids of  $\sim 5\%$  relative (Pertermann et al., 2008).

### 314 *Role of Simulation Cell Length ( $L_z$ )*

315 The thermal conductivity  $k$  exhibits a dependence on the size of the simulation  
316 cell in the direction of the heat flux  $L_z$  when the size of the simulation volume is of the  
317 same order as the longest phonon path length. This variation is explained by the increase  
318 in the number of active phonon modes available as the system size increases as well as  
319 the result of scattering that occurs at the interfaces of the heat source and sink in the  
320 NEMD system. The interface scattering effect is well known in MD studies and methods  
321 have been developed to account for it and hence obtain values of  $k$  appropriate for  
322 macroscopic systems (Chantrenne and Barrat, 2004; Varshney et al. 2009; Stackhouse  
323 and Stixrude, 2010). Finite-size effects are especially apparent in crystalline materials  
324 because the long-range order intrinsic to crystals gives rise to long mean free phonon path  
325 lengths that can exceed the size of the MD domain. In liquid and glassy materials, this is  
326 less of a problem because phonon mean free path lengths ( $\Lambda$ ) are of the same order as the  
327 scale of short range order, approximately 0.3-0.6 nm for typical silicate liquids and  
328 glasses without a great deal of variation (Kittel, 1949). Since the scale of short range  
329 order is considerably less than the size of a typical MD simulation box filled with  $\sim 10^4$   
330 atoms of  $\sim 5$ -10 nm in our simulations, finite-system-size effects are less pronounced  
331 compared to crystals. However, for good precision it is still desirable to account for  
332 finite-system-size effects since variations in  $L_z$  constrain the magnitudes of  $L_x$  and  $L_y$ ,

## Revision 2

333 necessarily, when tetragonal NEMD domains are utilized. The critical issue is the phonon  
334 mean free path length in an infinite (macroscopic) system ( $\Lambda_\infty$ ) relative to the z-  
335 dimension of the MD simulation box of length  $L_z$ . If the distance between the layers  
336 undergoing velocity exchange ( $L_z/2$ ) is comparable to  $\Lambda_\infty$ , an effective mean free path  $\Lambda_{\text{eff}}$   
337 can be defined (Schelling et al., 2002; Yoon et al., 2004) according to:

$$338 \quad \frac{1}{\Lambda_{\text{eff}}} = \frac{1}{\Lambda_\infty} + \frac{1}{L_z} \quad (5)$$

339 From kinetic theory, the phonon mean free path (MFP) is related to the sonic speed and  
340 specific isochoric heat capacity of the material by (Bridgman, 1914; Kittel and Kroemer,  
341 1980)

$$342 \quad k = \frac{1}{3} \rho C_V c \Lambda_{\text{eff}} \quad (6)$$

343 where  $\rho$  is the melt density ( $\text{kg/m}^3$ ),  $C_V$  is the isochoric specific heat capacity ( $\text{J/kg K}$ )  
344 and  $c$  is the sonic velocity ( $\text{m/s}$ ). Substituting Eq. (5) into Eq. (6) gives a relation between  
345  $k$  and  $L_z$ :

$$346 \quad \frac{1}{k} = A \left( \frac{1}{\Lambda_\infty} + \frac{1}{L_z} \right) \quad (7)$$

347  
348 where  $A = 3(\rho C_V c)^{-1}$  is constant at any given state point and composition. Eq. (7) is of  
349 the form  $1/k = C_1 + C_2/L_z$  where  $C_1$  and  $C_2$  are constants. To account for finite-system-  
350 size effects, NEMD conductivities from simulations performed in different sized boxes  
351 are plotted in  $1/k - 1/L_z$  coordinates. Extrapolation as  $1/L_z \rightarrow 0$  gives the desired value of  $k$   
352 applicable to a macroscopic system. All of the thermal conductivity values reported  
353 below for  $\text{Mg}_2\text{SiO}_4$ ,  $\text{CaMgSi}_2\text{O}_8$  and  $\text{NaAlSi}_3\text{O}_8$  have been analyzed as a function of

## Revision 2

354 simulation cell length as outlined above to obtain the desired macroscopic  $k$  from Eq. (7)  
355 using an optimal swap rates of  $\Omega \sim 20\text{-}40$  fs. Additional details on the NEMD method  
356 and statistical treatment of data may be found in Tikunoff (2013).

357

358

359

360

## RESULTS

361 Values of the thermal conductivity at all state points for all compositions  
362 including the fluctuations in  $T$  and  $P$  and the  $1\sigma$  uncertainties in  $k$  are collected in Tables  
363 1, 2 and 3 for  $\text{CaMgSi}_2\text{O}_6$ ,  $\text{NaAlSi}_3\text{O}_8$  and  $\text{Mg}_2\text{SiO}_4$ , respectively. Figure 2 illustrates the  
364 calculation of finite-size effects, where the inverse of the thermal conductivity as a  
365 function of simulation cell length is plotted for  $\text{CaMgSi}_2\text{O}_6$  at fixed  $P$  and  $T$ .  
366 Extrapolation of the regression line to an infinite size system gives the phonon thermal  
367 conductivity  $k=1.143 \pm 0.004$  ( $1 \sigma$ )  $\text{W/m K}$ . This compares to the laboratory value at  
368 2000 K and ambient pressure of  $1.159 \pm 0.058$  from Hofmeister et al. (2009) quite well.  
369 As another example, the NEMD value of  $k$  for diopside composition at 1763 K and 1-bar  
370 of  $1.186 \pm 0.019$   $\text{W/m K}$ , in this case uncorrected for a small finite-size effect, is within 1  
371 % of the laboratory value of  $1.178 \pm 0.06$   $\text{W/m K}$  also from Hofmeister et al. (2009).  
372 Finally, extrapolation of the 1800 K (1-bar) laboratory measurement for molten albite  
373 from Hofmeister et al (2009) gives a value of 1.55  $\text{W/m K}$  that can be compared to the  
374 NEMD value at 2091 K and 1-bar (Table 2) of 1.498  $\text{W/m K}$ . In conclusion, values  
375 computed for  $\text{NaAlSi}_3\text{O}_8$  and  $\text{CaMgSi}_2\text{O}_6$  compositions from NEMD compare well with  
376 laboratory results at ambient pressure. Evidently, the Matsui potential can recover  
377 accurate thermal conductivities at ambient pressure for these compositions. NEMD  
simulations for glassy materials, based on the criteria given earlier, are identified

## Revision 2

378 explicitly in the Tables. All others are for equilibrium or metastable liquids. Here we  
379 summarize the effects of T, P and composition on the thermal conductivity.

380 *CaMgSi<sub>2</sub>O<sub>6</sub>*

381 All calculated k values for CaMgSi<sub>2</sub>O<sub>6</sub> composition (both liquids and glass) are  
382 plotted on Figure 3. As T increases, k decreases, at all pressures although the effect is  
383 diminished as P increases. Figure 4 illustrates that a T increase from 3000 K to 4500 K  
384 decreases k by ~ 25 % from 1.02 W/m K to 0.72 in diopside liquid at ambient pressure.  
385 At higher pressure (~10 GPa), the T-dependence of k is substantially weaker. At ~ 20  
386 GPa, k depends weakly on temperature and assumes a value of ~2.4 W/m K (Table 1). In  
387 diopside liquid at 3500 K, a pressure increase from ambient to ~ 20 GPa increases k from  
388 ~1.15 W/m K to 2.5 W/m K, an increase of more than 100%. The increase in k with  
389 increasing P along an isotherm only slightly depends upon T. For example, at ~4500 K, k  
390 increases from 0.73 W/m K at ambient pressure to 2.28 W/m K at ~20 GPa, an increase  
391 by a factor greater than 3 which is comparable to the increase with pressure at lower T.

392 In summary, for CaMgSi<sub>2</sub>O<sub>6</sub> k decreases with increasing temperature along an  
393 isobar. The effect of increasing pressure on k along an isotherm is rather significant: a  
394 factor of ~ 2-3 as pressure increases from ambient to ~30 GPa. The trade-off between the  
395 opposing effects of increasing T and P on thermal conductivity for molten diopside can  
396 be evaluated by computing the change in k along the diopside liquid 2000 K isentrope.  
397 Temperature along the isentrope is given by  $T = T_0 \exp(\alpha P / \rho C_p)$ , where  $\alpha$  is the  
398 isobaric expansivity,  $\rho$  is the melt density and  $C_p$  is the isobaric specific heat capacity.  
399 Adopting MD-derived mean values of density, heat capacity and expansivity along the

## Revision 2

400 isentrope for liquid diopside from Creamer (2012), one finds that  $k$  increases by a factor  
401 of 2.2 as pressure increases to 30 GPa along the 2000 K isentrope.

### 402 *Liquid albite*

403         Albite liquid exhibits  $k$ - $P$ - $T$  dependence that is qualitatively similar to molten  
404 diopside; all values are listed in Table 2 and depicted in Figure 5. The thermal  
405 conductivity decreases with increasing  $T$  along an isobar and strongly increases as  
406 pressure increases along an isotherm. For example, at  $\sim 4000$  K,  $k$  increases from 0.9 to  
407 2.6 W/m K from near ambient pressure to  $\sim 30$  GPa whereas at ambient  $P$ , in the  $T$  range  
408 2100-4024 K,  $k$  decreases from 1.45 W/m K to 0.89 W/m K. Similarly, at  $\sim 30$  GPa, as  $T$   
409 increases in the sequence 2060 K, 3068 K, 4034 K, thermal conductivity decreases in the  
410 sequence 2.88 W/m K, 2.72 W/ m K, 2.60 W/m K, respectively. In general, thermal  
411 conductivity for albite liquid exceeds that for liquid diopside when compared at identical  
412 (or nearly so)  $T$ - $P$  conditions, although differences become smaller as  $P$  increases.

### 413 *Liquid forsterite*

414         Liquid forsterite shows the strongest negative correlation of  $k$  with  $T$  at ambient  
415 pressure of the three liquid compositions studied. The conductivity decreases from 1.37  
416 W/ m K at 2560 K to 0.68 W/ m K at 4580 K (Figure 6). Similar to the other  
417 compositions, along an isotherm,  $k$  increases substantially as pressure increases (Figure  
418 7). For example, at  $\sim 3550$  K,  $k$  increases from 0.90 W/ m K to 2.12 W/ m K as pressure  
419 increases from ambient to from ambient to 11 GPa pressure, an increase by a factor of  
420 2.4, similar to the behavior in diopside and albite melts.

### 421 *Glass*

## Revision 2

422 For  $\text{CaMgSi}_2\text{O}_6$  at 2076 K and 2551 K and for  $\text{NaAlSi}_3\text{O}_8$  at 2070 K and 3056 K,  
423 the temperature is below the computer glass transition at all pressures. For glassy  
424 diopside at fixed pressure, there is a very slight T-dependence of k such that as T  
425 increases, k decreases. In contrast, along an isotherm k increases appreciably as pressure  
426 increases. For example, at T=2076 K, k increases from 1.14 W/m K at zero pressure to  
427 2.89 W/ m K at ~30 GPa, an increase by a factor of ~ 2.5. Glassy albite exhibits similar  
428 behavior: a weak, almost negligible, negative dependence of thermal conductivity with  
429 temperature but a rather strong increase in k as pressure increases along an isotherm. The  
430 weak isobaric thermal dependence of the thermal conductivity of albite and diopside  
431 glass is consistent with the experimental findings of Hofmeister et al (2009) as is the  
432 observation that glass k values are larger than values for corresponding liquids when  
433 compared at temperatures around the glass transition. Because the properties of a glass  
434 depend on its preparation (thermal) history, direct comparison between NEMD values  
435 and laboratory results is not meaningful given the enormously different cooling rates  
436 during preparation of computer versus laboratory glasses. Additional NEMD simulations  
437 on the glasses are needed to quantify the effects of preparation history on glass thermal  
438 conductivity. Diopsidic and albitic glasses have thermal conductivities of  $k=1.14$  W/m K  
439 and  $k=1.50$  W/m K, respectively, at similar state points (e.g., T=2059 ±12 K, P=-0.04  
440 ±0.14 GPa and T=2091 ±20 K, P=0.20 ±0.23 GPa, respectively). The more polymerized  
441  $\text{NaAlSi}_3\text{O}_8$  composition in which, to first order, each oxygen has two nearest neighbors  
442 of Si and/or Al (at low pressure) is a better thermal conductor than the less polymerized  
443 composition  $\text{CaMgSi}_2\text{O}_6$  in which, to first order, two of the three oxygens of the  
444 metasilicate ( $\text{SiO}_3$ ) backbone have one nearest neighbor of Si and the remaining oxygen

## Revision 2

445 is bridging oxygen. The relationship between glass or melt atomic structure and phonon  
446 conductivity is discussed more fully in Part II. Here we note that as pressure increases,  
447 this effect becomes quantitatively muted since, at high pressures structures approximately  
448 converge being dominated by high coordination numbers.

449

450

## IMPLICATIONS

451 Although quantitative knowledge of the effects of temperature, pressure and  
452 composition on the phonon conductivity of silicate liquids is critical for the analysis of  
453 many geophysical and petrological problems, very few measurements exist due to  
454 experimental difficulties. There are virtually no measurements on the effects of pressure  
455 on thermal conductivity of silicate liquids that we are aware of. In this study, we have  
456 implemented a Nonequilibrium Molecular Dynamics technique within the context of  
457 classical Molecular Dynamics to study the phonon conductivities of amorphous (molten  
458 and glassy)  $\text{Mg}_2\text{SiO}_4$ ,  $\text{CaMgSi}_2\text{O}_6$  and  $\text{NaAlSi}_3\text{O}_8$  at elevated temperatures (2500-4500  
459 K) and pressures (0-30 GPa) and provide estimates of this important geophysical  
460 parameter in these liquids. The NEMD method takes account of finite-size effects and  
461 faithfully captures experimental thermal conductivities for simple fluids such as Ar and  
462 alkali halide liquids. The NEMD results compare very well with ambient pressure  
463 experimental values for liquid  $\text{CaMgSi}_2\text{O}_6$  and  $\text{NaAlSi}_3\text{O}_8$  from Hofmeister et al (2009).  
464 For example, experimental values at 1-bar for  $\text{CaMgSi}_2\text{O}_6$  and  $\text{NaAlSi}_3\text{O}_8$  at 2000 K of  
465 1.15 W/m K and 1.55 W/m K compare well with the NEMD values at the same state  
466 point of 1.14 W/m K and 1.45 W/m K, respectively. In the temperature range of this  
467 study all compositions exhibit a negative dependence of  $k$  with temperature and a strong

## Revision 2

468 positive dependence of  $k$  with pressure. There is also a discernable effect at low pressure  
469 and identical temperatures such that the thermal conductivity increases as the extent of  
470 polymerization increases. For example, molten albite, exhibits a greater thermal  
471 conductivity than molten  $\text{Mg}_2\text{SiO}_4$  when compared at comparable state points. As  
472 pressure increases this polymerization effect is damped presumably because the effect of  
473 pressure is to increase the coordination number of oxygen around a central Si and  
474 likewise the coordination number of Si and other cations around a central oxygen. As  
475 pressure increases, all compositions become closer in structure and hence the structural  
476 control on thermal conductivity diminishes. In part II of this study, the MD-derived  
477 thermal conductivities are related to macroscopic thermodynamic properties and melt  
478 structures.  
479  
480

## Revision 2

### 481 **References**

- 482  
483 Allwardt, J.R., Stebbins, J., Terasaki, H., Du, Lin-Shu, Frost, D.J., Withers, A.C.,  
484 Hirschmann, M.M., Suzuki, A., and Ohtani, E. (2007) Effect of structural transitions on  
485 properties of high-pressure silicate melts; <sup>27</sup>Al NMR, glass densities, and melt viscosities.  
486 American Mineralogist, 92, 1093-1104.  
487  
488 Anzellini, S., Dewaele, A., Mezouar, M., Loubeyre, P., and Morard, G. (2013) Melting of  
489 Iron at Earth's Inner Core Boundary Based on Fast X-ray Diffraction. Science, 340, 464-  
490 466.  
491  
492 Arndt, J., and Häberle, F. (1973) Thermal expansion and glass transition temperatures of  
493 synthetic glasses of plagioclase-like compositions. Contributions to Mineralogy and  
494 Petrology, 39, 175-183.  
495  
496 Beck, P., Goncharov, A.F., Struzhkin, V., Militzer, B., Mao, H.-K., and Hemley, R.J.  
497 (2007) Measurement of thermal diffusivity at high pressure using a transient heating  
498 technique. Applied Physics Letters, 91, 181914-(1-3).  
499  
500 Bedrov, D., Smith, G.D., and Sewell, T.D. (2000) Thermal conductivity of liquid  
501 octahydro-1,3,5,7-tetranitro-1,3,5,7-tetrazocine (HMX) from molecular dynamics  
502 simulations. Chemical Physics Letters, 324, 64-68.  
503  
504 Bridgman, P.W. (1914) A complete collection of thermodynamic formulas. Physical  
505 Review, 3, 273-281.  
506  
507 Cao, B.Y. (2008) Nonequilibrium molecular dynamics calculation of the thermal  
508 conductivity based on an improvised relaxation scheme. The Journal of Chemical  
509 Physics, 129, 074106 1-8.  
510  
511 Chantrenne, P., and Barrat, J.-L. (2004) Finite size effects in determination of thermal  
512 conductivities: comparing molecular dynamics results with simple models. Journal of  
513 Heat Transfer, 126, 577-585.  
514  
515 Creamer, J. (2012) Modeling fluid-rock Interaction, melt-rock interaction, and silicate  
516 melt properties at crustal to planetary interior conditions. PhD. thesis, University of  
517 California, Santa Barbara, 117 p.  
518  
519 Daniel, I., Gillet, P., McMillan, P.F., and Poe, B.T. (1996) Raman spectroscopic study of  
520 structural changes in calcium aluminate (CaAl<sub>2</sub>O<sub>4</sub>) glass at high pressure and high  
521 temperature. Chemical Geology, 128, 5-15.  
522  
523 de Koker, N., Steinle-Neumann, G., and Vlcek, V. (2012) Electrical resistivity and  
524 thermal conductivity of liquid Fe alloys at high P and T, and heat flux in the Earth's core.  
525 Proceedings of the National Academy of Sciences, 109, 4070-4073.  
526

## Revision 2

- 527 Degiovanni A., Andre S., and Maillet D. (1994) Phonic conductivity measurement of a  
528 semi-transparent material. In: Tong TW (ed) Thermal conductivity 22. Technomic,  
529 Lancaster, PN, pp 623-633.  
530
- 531 Donth, E-J. (2001) Relaxation Dynamics in Liquids and Disordered Materials. Springer  
532 Series in Materials Science, 48, 419.  
533
- 534 Galamba, N., Nieto de Castro, C.A., and Ely, J.F. (2004) Thermal conductivity of molten  
535 alkali halides from equilibrium molecular dynamics simulations. Journal of Chemical  
536 Physics, 120, 8676-8682.  
537
- 538 Ghiorso M., and Spera F. (2009) Large scale simulations. Reviews of Mineralogy and  
539 Geochemistry, 71, 437-463 (eds. R. Wentzcovitch and L. Stixrude). Mineralogical  
540 Society of America.  
541
- 542 Giordano, D., and Dingwell, D. B. (2003) The kinetic fragility of natural silicate melts.  
543 Journal of Physics: Condensed Matter, 15, S945.  
544
- 545 Hammerschmidt, U., and Sabuga, W. (2000) Transient Hot Wire Method (THW):  
546 Uncertainty Assessment. International Journal of Thermophysics, 21, 1255-78.  
547
- 548 Healy, J.J, de Groot, J.J, and Kestin, J. (1976) The Theory of the Transient Hot-Wire  
549 Method for Measuring Thermal Conductivity. Physica C, 82, 392-408.  
550
- 551 Hernlund, J., and Jellinek, A. (2010) Dynamics and structure of a stirred partially molten  
552 ultralow-velocity zone. Earth and Planetary Science Letters, 296, 1-8.  
553
- 554 Hofmeister, A. (2007) Pressure dependence of thermal transport properties. Proceedings  
555 of the National Academy of Sciences, 104, 9192-7.  
556
- 557 Hofmeister, A.M., Whittington, A.G., and Pertermann, M. (2009). Transport properties of  
558 high albite crystals and near-end member feldspar and pyroxene glasses and melts to high  
559 temperature. Contributions to Mineralogy and Petrology, 158, Pp. 381-400.  
560
- 561 Idehara, K. (2011) Structural heterogeneity of an ultra-low-velocity zone beneath the  
562 Philippine Islands: Implications for core-mantle chemical interactions induced by  
563 massive partial melting at the bottom of the mantle. Physics of the Earth and Planetary  
564 Interiors, 184, 80-90.  
565
- 566 Kang, Y., and Morita, K. (2006) Thermal Conductivity of the CaO-Al<sub>2</sub>O<sub>3</sub>-SiO<sub>2</sub> System.  
567 Iron and Steel Institute of Japan International, 46, 420-426.  
568
- 569 Karki, B. B., Bohara, B., and Stixrude, L. (2011) First-principles study of diffusion and  
570 viscosity of anorthite (CaAl<sub>2</sub>Si<sub>2</sub>O<sub>8</sub>) liquid at high pressure. American Mineralogist, 96,  
571 744-751.  
572

## Revision 2

- 573 Kittel, C. (1949) Interpretation of the thermal conductivity of glasses. *Physical Review*  
574 *Series II*, 75, 972-974.  
575
- 576 Kittel, C., and Kroemer, H. (1980) *Thermal Physics*. W. H. Freeman and Company.  
577
- 578 Kubo, R. (1966) The fluctuation-dissipation theorem. *Reports on Progress in Physics*, 29,  
579 255-284.  
580
- 581 Langer, J.S. (2014) Theories of glass formation and the glass transition. *Reports on*  
582 *Progress in Physics*, 77, 042501.  
583
- 584 Lee, H. L., and Hasselman, D.P.H. (1985) Comparison of Data for Thermal Diffusivity  
585 Obtained by Laser-Flash Method Using Thermocouple and Photodetector. *Journal of the*  
586 *American Ceramic Society*, 68, C-12–C-13.  
587
- 588 Martin, B., Spera, F.J., Ghiorso, M., and Nevins, D. (2009) Structure, thermodynamic  
589 and transport properties of molten  $Mg_2SiO_4$ : Molecular dynamics simulations and model  
590 EOS. *American Mineralogist*, 94, 693-703.  
591
- 592 Martin G.B., Ghiorso, M., and Spera, F. (2012) Transport properties and equation of  
593 state of 1-bar eutectic melt in the system  $CaAl_2Si_2O_8$ - $CaMgSi_2O_6$  by molecular  
594 dynamics simulation. *American Mineralogist*, 97, 1155-1164.  
595
- 596 Martinez, L.M., and Angell, C.A. (2001) A thermodynamic connection to the fragility of  
597 glass-forming liquids. *Nature*, 410, 663-667.  
598
- 599 Matsui M. (1998) Computational modeling of crystals and liquids in the system  $Na_2O$ -  
600  $CaO$ - $MgO$ - $Al_2O_3$ - $SiO_2$ . In *Properties of Earth and Planetary Materials at High Pressure*  
601 *and Temperature* (eds. M. H. Manghnani and T. Yagi). AGU, Washington, DC, pp. 145-  
602 148.  
603
- 604 McBirney, A., and Murase, T. (1973) Rheological Properties of Magma. *Annual Review*  
605 *of Earth and Planetary Sciences*, 12, 337-357.  
606
- 607 Mehling, H., Hautzinger, G., Nilsson, O., Fricke, J., Hofmann, R., and Hahn, O. (1998)  
608 Thermal Diffusivity of Semitransparent Materials Determined by the Laser-Flash Method  
609 Applying a New Analytical Model. *International Journal of Thermophysics*, 19, 941-949.  
610
- 611 Metzler, R., and Klafter, J. (2004) The restaurant at the end of the random walk: recent  
612 developments in the description of anomalous transport by fractional dynamics. *Journal*  
613 *of Physics A: Mathematical and General*, 37, R161-R208.  
614
- 615 Morgan, N. A., and Spera, F. J. (2001) A molecular dynamics study of the glass transition  
616 in  $CaAl_2Si_2O_8$ : Thermodynamics and tracer diffusion. *American Mineralogist*, 86, 915-  
617 926.  
618

## Revision 2

- 619 Müller-Plathe, F. (1997) A simple nonequilibrium molecular dynamics method for  
620 calculating the thermal conductivity. *Journal of Chemical Physics*, 106, 6082-85.  
621
- 622 Müller-Plathe, F., and Bordat, P. (2004) *Novel Methods in Soft Matter Simulations*,  
623 edited by M. Karttunen, I. Vattulainen, and A. Lukkarinen, Lecture Notes in Physics Vol.  
624 640. Springer, Heidelberg, Germany.  
625
- 626 Mysen, B.O., and Richet, P. (2005) *Silicate Glasses and Melts, Properties and Structure*.  
627 Elsevier, Amsterdam, Pp. 544.  
628
- 629 Nevins, D., Spera, F.J., and Ghiorso, M. (2009) Shear Viscosity and diffusion in liquid  
630 MgSiO<sub>3</sub>: Transport properties and implications for terrestrial planet magma oceans.  
631 *American Mineralogist*, 94, 975-980.  
632
- 633 Olsen, P. (2013) The geodynamo's unique longevity. *Physics Today* 66, 11, 30.  
634
- 635 Passaglia, E., and Martin, G.M. (1964) Variation of glass temperature with pressure in  
636 polypropylene. *The Journal of Research of the National Institute of Standards and*  
637 *Technology*, 68A, 273.  
638
- 639 Pertermann, M., and Hofmeister, A. (2006) Thermal diffusivity of Olivine-group  
640 minerals at high temperature. *American Mineralogist*, 91, 1747-1760.  
641
- 642 Pertermann, M., Whittington, A.G., Hofmeister, A.M., Spera, F., and Zayak, J. (2008)  
643 Transport properties of low-sanidine single-crystals, glasses and melts at high  
644 temperature. *Contributions to Mineralogy and Petrology*, 155, 689-702.  
645
- 646 Rapaport D. C. (1995) *The Art of Molecular Dynamics Simulation*. Cambridge  
647 University Press.  
648
- 649 Reinsch, S., Nacimiento, M.L.F., Muller, R., and Zanotto, E.D. (2008) Crystal growth  
650 kinetics in cordierite and diopside glasses in wide temperature ranges. *Journal of Non-*  
651 *Crystalline Solids*, 354, 5386-5394.  
652
- 653 Roland, C.M., Hensel-Bielowka, S., Paluch, M., and Casalini, R. (2005) Supercooled  
654 dynamics of glass-forming liquids and polymers under hydrostatic pressure. *Reports on*  
655 *Progress in Physics*, 68, 140.  
656
- 657 Rosenfeld, Y., and Tarazona, P. (1998) Density functional theory and the asymptotic high  
658 density expansion of the free energy of classical solids and fluids. *Molecular Physics: An*  
659 *International Journal at the Interface Between Chemistry and Physics*, 95, 141-150.  
660
- 661 Schelling, P.K., Phillpot, S.R., and Keblinski, P. (2002) Comparison of atomic-level  
662 simulation methods for computing thermal conductivity. *Physical Review B*, 65, 144306  
663 1-12.  
664

## Revision 2

- 665  
666 Spera, F.J., Nevins, D., Ghiorso, M.S., and Cutler, I. (2009) Structure, thermodynamics  
667 and transport properties of  $\text{CaAl}_2\text{Si}_2\text{O}_8$  liquid. Part I: Molecular dynamics simulations.  
668 *Geochimica et Cosmochimica Acta*, 73, 6918-6936.  
669  
670 Spera, F.J., Ghiorso, M. S., and Nevins, D. (2011) Structure, thermodynamic and  
671 transport properties of liquid  $\text{MgSiO}_3$ : Comparison of molecular models and laboratory  
672 results. *Geochimica et Cosmochimica Acta*, 75, 1272-1296.  
673  
674 Stackhouse, S and Stixrude, L. (2010) Theoretical Methods for Calculating the Lattice  
675 Thermal Conductivity of Minerals. *Reviews in Mineralogy & Geochemistry*. 71, 253-  
676 269.  
677  
678 Stixrude, L., de Koker, N., Sun, N., Mookherjee, M., and Karki, B.B. (2009)  
679 Thermodynamics of silicate liquids in the deep Earth. *Earth and Planetary Science Letters*,  
680 278, 226-232.  
681  
682 Sun, N., Stixrude, L., de Koker, N., and Karki, B.B. (2011) First principles molecular  
683 dynamics simulations of diopside ( $\text{CaMgSi}_2\text{O}_6$ ) liquid to high pressure. *Geochimica et*  
684 *Cosmochimica Acta*, 75, 3792-3802.  
685  
686 Terao, T., Lussetti, E., and Müller-Plathe F. (2007) Nonequilibrium molecular dynamics  
687 methods for computing the thermal conductivity: application to amorphous polymers.  
688 *Physical Review E*, 75.  
689  
690 Tikunoff, D. (2013) Composition, Temperature and Pressure Dependence of the Phonon  
691 (Thermal) Conductivity of Silicate Geoliquids. M.S. thesis, University of California,  
692 Santa Barbara, 73 p.  
693  
694 Tritt T.M., and Weston D. (2004) Measurement techniques and considerations for  
695 determining thermal conductivity of bulk materials. Tritt T.M., *Thermal conductivity*  
696 *theory, properties, and applications*, Kluwer Academic/Plenum Publishers, New York,  
697 187–203.  
698  
699 Varshney, V., Patnaik, S., Roy, A., and Farmer, B. (2009) Heat Transport in Epoxy  
700 Networks: a Molecular Dynamics Study. *Polymer*, 50, 3378-3385.  
701  
702 Vogelsang, R., Hoheisel, C. and Ciccotti, G. (1987) Thermal conductivity of the  
703 Lennard-Jones liquid by molecular dynamics calculations. *The Journal of Chemical*  
704 *Physics*, 86, 6371-6375.  
705  
706 Wang, B., Kuo, J., Bae, S., and Granick, S. (2012) When Brownian Diffusion is not  
707 Gaussian. *Nature Materials*, 11, 481.  
708  
709 Weeks, E. R., and Weitz D.A. (2002) Subdiffusion and the cage effect studied near the  
710 colloidal glass transition. *Journal of Chemical Physics*, 284, 361-367.

## Revision 2

711

712 Wen, L., and Helmberger, D. (1998) Ultra-Low Velocity Zones Near the Core-Mantle  
713 Boundary from Broadband PKP Precursors. *Science*, 279, 1701-1703.

714

715 Whittington, A., Hofmeister, A., and Nabelek, P. (2009) Temperature Dependent  
716 Thermal Diffusivity of the Earth's Crust and Implications for Magmatism. *Nature*, 458,  
717 319-321.

718

719 Yoon, Y.G., Car, R., Srolovitz, D.J., and Scandolo, S. (2004) Thermal conductivity of  
720 crystalline quartz from classical simulations. *Physical Review B*, 70, 012302 1-4.

721

722

723

724

725

726

727

728

## Revision 2

### 729 **Figure Legends**

730

731 **Figure 1:** Phonon thermal conductivity of  $\text{CaMgSi}_2\text{O}_6$  ( $\rho=2569 \text{ kg/m}^3$  at  $P=0.36 \pm 0.17$   
732 GPa and  $T=1764 \pm 13 \text{ K}$ ) versus particle swap time interval  $\Omega$  in femtoseconds. Aspect  
733 ratio of the NEMD box equals unity (i.e.,  $k$  has not been corrected for finite-system-size  
734 effects). For large values of  $\Omega$ , the uncertainty in  $k$  is relatively large although its mean  
735 value is not very different from the best estimate of  $1.154 \pm 0.02 \text{ W/m K}$  at  $\Omega=20$ . The  
736 laboratory value from Hofmeister et al. (2009) at 1764 K and 1 bar is  $1.17 \pm 0.06 \text{ W/m K}$ .  
737 Applying a finite-system-size correction increases the value of  $k$  whereas the effect of  
738 pressure is to increase  $k$  from its one-bar value. These effects approximately cancel in  
739 this case. In the remainder of this work the duration between swap events is between 10  
740 and 30 fs, and the total duration of NEMD simulation is 2 ns.

741

742 **Figure 2:** Inverse phonon thermal conductivity ( $k^{-1}$ ) versus inverse system cell length  $L_z$   
743 for  $\text{CaMgSi}_2\text{O}_6$  at  $T=2060 \pm 15 \text{ K}$ ,  $P= -0.04 \pm 0.15 \text{ GPa}$  and  $\rho=2392 \text{ kg/m}^3$ . Extrapolation  
744 in the limit  $L_z \rightarrow 0$ , the intercept, gives the value  $k=1.143 \pm 0.004 \text{ W/m K}$ . This can be  
745 compared to the laboratory value at 2000 K and ambient pressure of  $1.159 \pm 0.058$  from  
746 Hofmeister et al. (2009). The number of particles  $N$  used in the simulations for  $L_z = 4.22$   
747 nm, 8.44 nm, 12.66 nm and 16.88 nm are 5000, 10000, 15000 and 20000, respectively. In  
748 all cases the swap time interval is  $\Omega= 20 \text{ fs}$  and the total simulation duration  $t_D= 2 \text{ ns}$ .

749

750 **Figure 3:** Thermal conductivity for amorphous diopside (glass and liquid) versus  
751 pressure along quasi-isotherms  $\sim 2000 \text{ K}$ ,  $2500 \text{ K}$ ,  $3500 \text{ K}$  and  $4500 \text{ K}$ . Raw data is in  
752 Table 1. Data at the highest pressure are near the limits of the classical potential used in  
753 the simulations and are included for the purposes of completeness.

754

755 **Figure 4:** Variation of thermal conductivity at ambient conditions and at 10 GPa for  
756  $\text{CaMgSi}_2\text{O}_6$  composition. The effect of  $T$  on  $k$  is muted as pressure increases.

757

758 **Figure 5:** Thermal conductivity for amorphous albite (glass and liquid) versus pressure  
759 along three quasi-isotherms at  $\sim 2000 \text{ K}$ ,  $3000 \text{ K}$  and  $4000 \text{ K}$ . Raw data can be found in  
760 Table 2.

761

762 **Figure 5:** Thermal conductivity for amorphous albite (glass and liquid) versus pressure  
763 along three quasi-isotherms at  $\sim 2000 \text{ K}$ ,  $3000 \text{ K}$  and  $4000 \text{ K}$ . Raw data can be found in  
764 Table 2.

765

766 **Figure 6:** Thermal conductivity of molten  $\text{Mg}_2\text{SiO}_4$  at  $P = 0.07 \pm 0.16 \text{ GPa}$  as a function  
767 of temperature.

768

769 **Figure 7:** Thermal conductivity of molten  $\text{Mg}_2\text{SiO}_4$  as a function of pressure along the  
770  $T = 3548 \pm 18 \text{ K}$  isotherm.

771

772

773

774

775

Revision 2

776 **TABLES**

777 **Table 1:** NEMD results for liquid and glassy CaMgSi<sub>2</sub>O<sub>6</sub>. Temperatures in bold are  
 778 averages used in the Figures. 1 $\sigma$  fluctuations are reported for T and P of the NEMD run.  
 779 1 $\sigma$  errors for k are found by propagation of error of the computed T gradient and the  
 780 deviation from linearity in 1/k versus 1/L<sub>z</sub>.

781  
 782

Density (kg/m <sup>3</sup> )	T (K)	$\sigma_T$ (K)	P (GPa)	$\sigma_P$ (GPa)	k (W/m K)	$\sigma_k$ (W/m K)	State
2392.49	2059	12.31	-0.04	0.14	1.143	0.002	Glass
2936.33	2067	11.07	5.24	0.16	1.585	0.009	Glass
3199.44	2084	11.93	10.09	0.17	2.023	0.067	Glass
3593.14	2075	15.85	20.20	0.26	2.262	0.060	Glass
3882.94	2096	12.55	31.63	0.15	2.870	0.113	Glass
	<b>2076</b>						
2287.70	2519	30.38	0.13	0.33	1.194	0.040	Glass
2842.69	2554	18.21	5.27	0.21	1.611	0.087	Glass
3115.19	2559	18.47	10.07	0.27	1.914	0.057	Glass
3543.53	2561	18.11	21.51	0.27	2.400	0.099	Glass
3800.88	2561	22.28	31.30	0.35	2.265	0.067	Glass
	<b>2551</b>						
2250.00	2815	13.60	0.37	0.13	1.088	0.022	Liquid
3107.01	2812	17.00	10.80	0.25	1.990	0.004	Liquid
2130.00	3055	14.57	0.18	0.13	1.018	0.003	Liquid
3047.07	3060	19.88	10.39	0.23	1.942	0.022	Liquid
1990.00	3300	15.89	0.03	0.12	0.899	0.006	Liquid
3017.68	3295	21.26	10.51	0.25	1.930	0.002	Liquid
2043.78	3558	22.13	0.43	0.16	0.977	0.007	Liquid
2770.78	3562	12.01	6.82	0.12	1.903	0.005	Liquid
2931.74	3540	22.92	9.59	0.28	1.862	0.014	Liquid
3354.22	3516	31.20	20.24	0.38	2.495	0.099	Liquid
3618.39	3523	28.35	30.10	0.36	3.045	0.110	Liquid
	<b>3540</b>						
1570.00	3814	19.26	-0.13	0.10	0.675	0.012	Liquid
2950.00	3784	17.60	10.69	0.19	1.892	0.002	Liquid
1770.00	4053	20.00	0.23	0.12	0.801	0.001	Liquid
2910.00	4037	18.81	10.64	0.19	1.962	0.005	Liquid
1730.00	4304	20.82	0.35	0.12	0.768	0.011	Liquid

Revision 2

2870.00	4313	21.92	10.64	0.21	1.850	0.041	Liquid
1625.79	4527	28.72	0.33	0.15	0.717	0.014	Liquid
2506.22	4521	36.77	5.40	0.30	1.437	0.024	Liquid
2824.53	4525	30.94	10.38	0.27	1.847	0.072	Liquid
3199.46	4525	38.37	19.71	0.41	2.280	0.145	Liquid
3494.87	4488	44.71	30.18	0.52	2.292	0.093	Liquid
	4517						

783  
784  
785  
786

Revision 2

787  
 788  
 789  
 790  
 791  
 792  
 793

**Table 2:** NEMD results for liquid and glassy NaAlSi<sub>3</sub>O<sub>8</sub>. Temperatures in bold are averages used in the Figures. 1 $\sigma$  fluctuations are reported for T and P of the NEMD run. 1 $\sigma$  errors for k are found by propagation of error of the computed T gradient and the deviation from linearity in 1/k versus 1/L<sub>z</sub>.

Density (kg/m <sup>3</sup> )	T (K)	$\sigma_T$ (K)	P (GPa)	$\sigma_P$ (GPa)	k (W/mK)	$\sigma_k$ (W/mK)	State
2313.68	2091	20.30	0.20	0.23	1.454	0.083	Glass
2786.85	2057	23.56	4.96	0.36	1.959	0.028	Glass
3072.49	2078	19.75	10.22	0.33	2.161	0.133	Glass
3487.10	2064	17.75	21.51	0.31	2.381	0.089	Glass
3698.19	2060	19.00	29.61	0.28	2.883	0.152	Glass
	<b>2070</b>						
2093.73	3062	19.90	0.04	0.19	0.989	0.036	Glass
2737.45	3057	23.72	6.05	0.29	1.768	0.093	Glass
2960.77	3047	24.97	10.31	0.30	2.548	0.135	Glass
3271.26	3046	23.22	18.65	0.34	2.294	0.059	Glass
3578.91	3068	19.05	30.55	0.30	2.716	0.142	Glass
	<b>3056</b>						
1841.85	4024	43.56	0.22	0.27	0.888	0.033	Liquid
2550.35	4013	37.82	5.11	0.37	1.652	0.098	Liquid
2803.67	3996	33.72	9.42	0.43	1.884	0.055	Liquid
3250.39	4016	36.07	21.88	0.48	2.417	0.022	Liquid
3464.66	4034	30.61	30.72	0.39	2.597	0.206	Liquid
	<b>4017</b>						

794  
 795  
 796  
 797  
 798  
 799  
 800  
 801

Revision 2

802  
803  
804  
805  
806  
807  
808

**Table 3:** NEMD results for liquid Mg<sub>2</sub>SiO<sub>4</sub> thermal conductivity values. Temperatures and Pressures in bold are averages used in the Figures. 1 $\sigma$  fluctuations are reported for T and P of the NEMD run. 1 $\sigma$  errors for k are found by propagation of error of the computed T gradient and the deviation from linearity in 1/k versus 1/L<sub>z</sub>.

Density (kg/m <sup>3</sup> )	T (K)	$\sigma_T$ (K)	P (GPa)	$\sigma_P$ (GPa)	k (W/mK)	$\sigma_k$ (W/mK)
2324.97	2549	12.51	0.02	0.14	1.364	0.009
2163.23	2723	27.75	-0.35	0.26	1.163	0.020
2163.23	3023	30.64	0.09	0.27	1.170	0.038
2031.11	3289	16.77	0.00	0.13	1.056	0.005
1825.22	3555	18.67	-0.16	0.12	0.896	0.002
1939.27	3805	18.60	0.36	0.13	1.043	0.004
1798.12	4062	19.39	0.26	0.12	0.933	0.001
1588.67	4581	30.48	0.34	0.11	0.681	0.001
			<b>0.07</b>			
1825.22	3555	18.67	-0.16	0.12	0.896	0.002
2306.17	3567	19.63	1.79	0.15	1.292	0.008
2503.73	3552	16.96	3.51	0.17	1.629	0.013
2724.53	3528	17.79	6.28	0.18	1.825	0.023
2844.71	3535	18.21	8.32	0.19	1.936	0.023
2972.07	3554	17.97	10.96	0.20	2.114	0.005
	<b>3548</b>					

809  
810

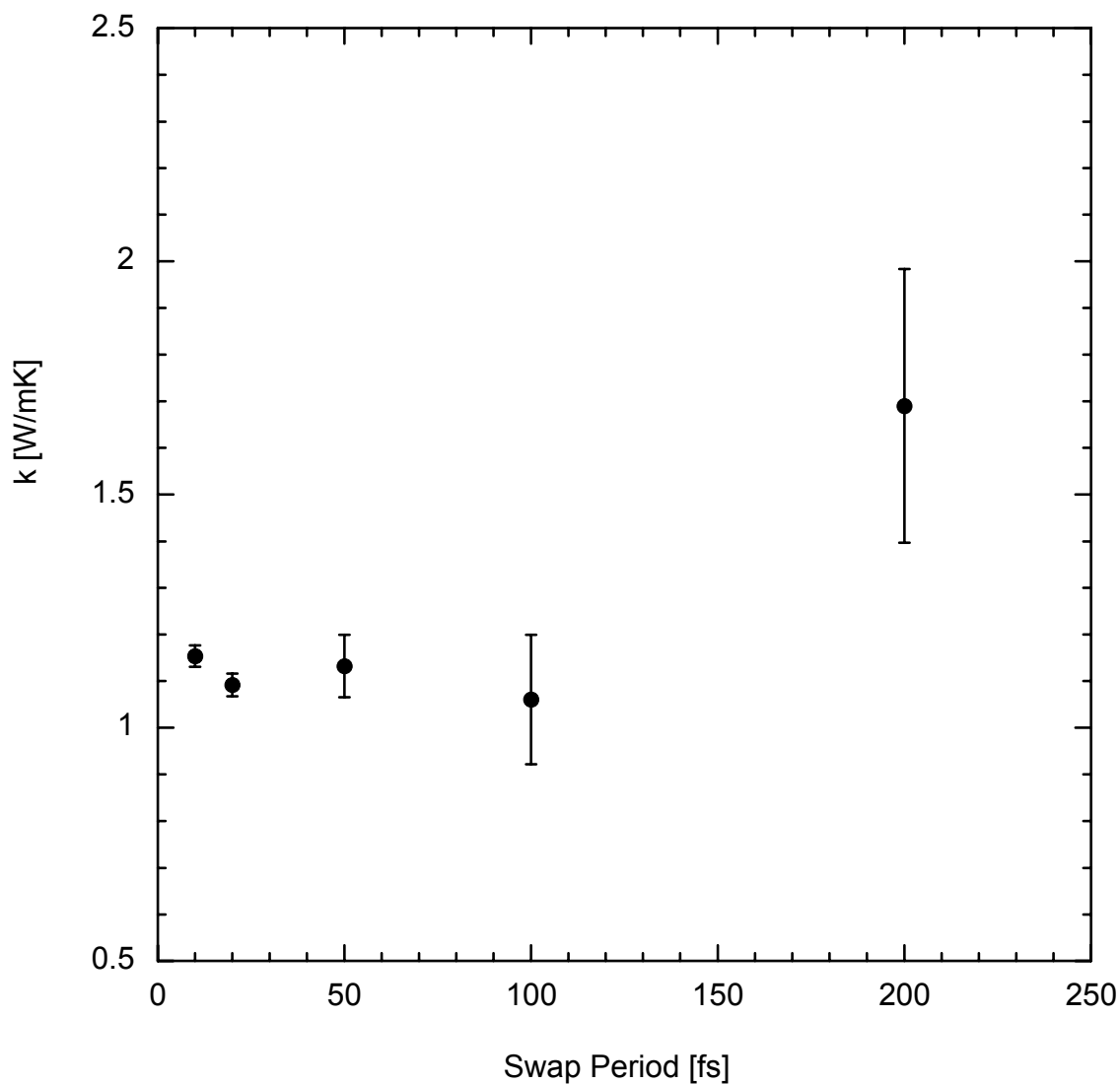
Revision 2

811

## 812 FIGURES

813

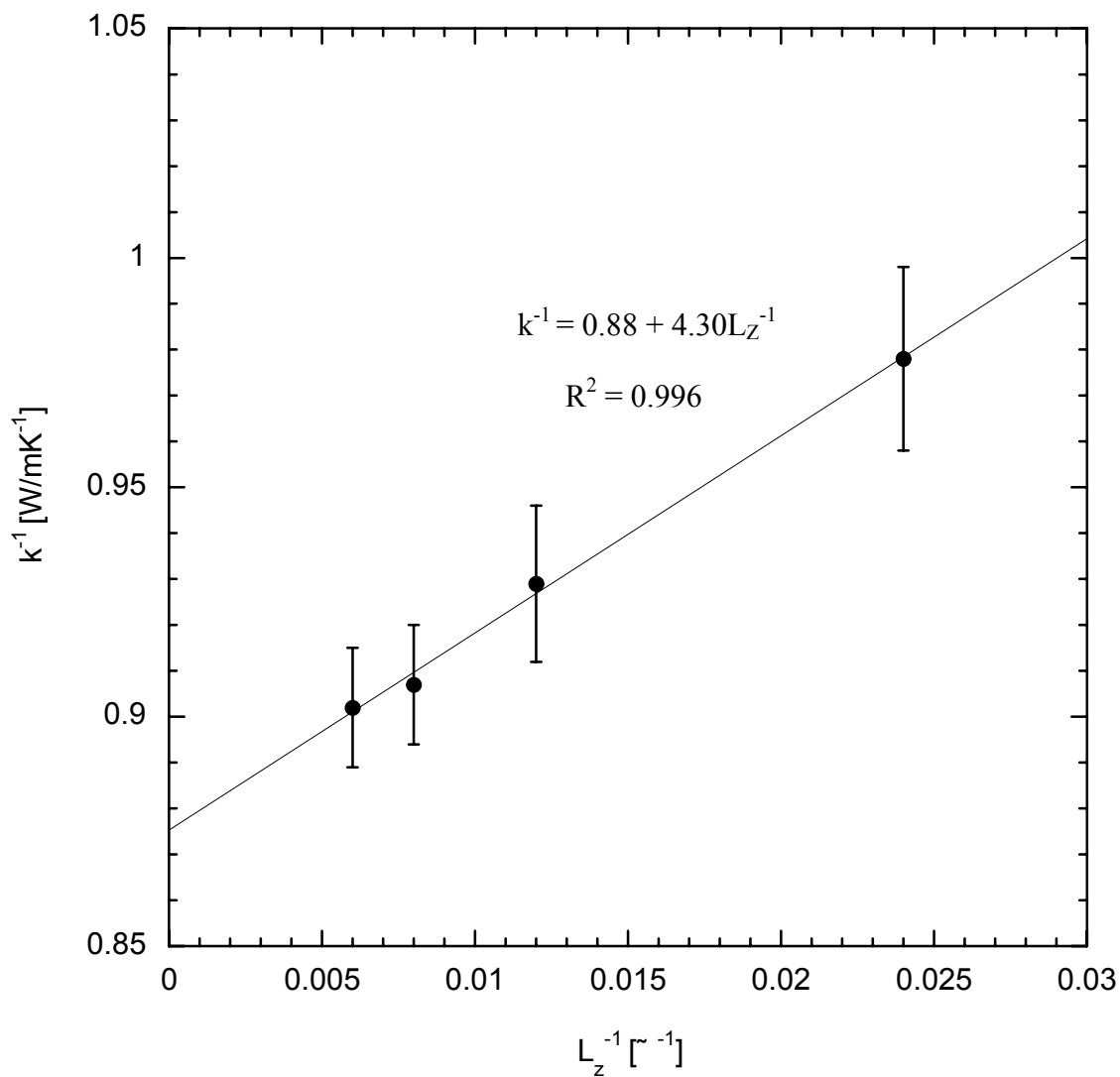
814 **Figure 1**



815

Revision 2

816 **Figure 2**



817

818

819

820

821

822

823

824

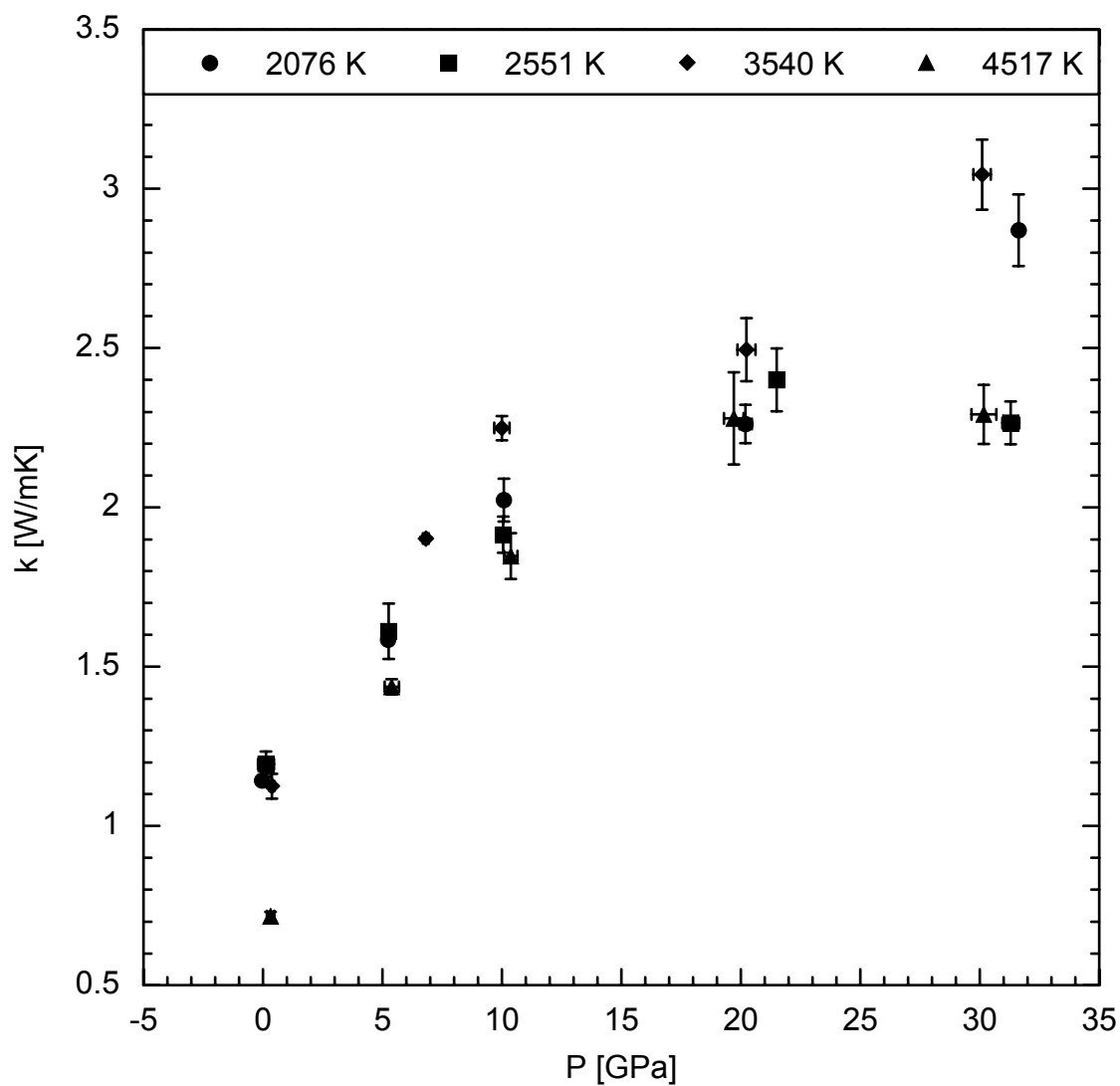
825

826

827

Revision 2

828 **Figure 3**



829

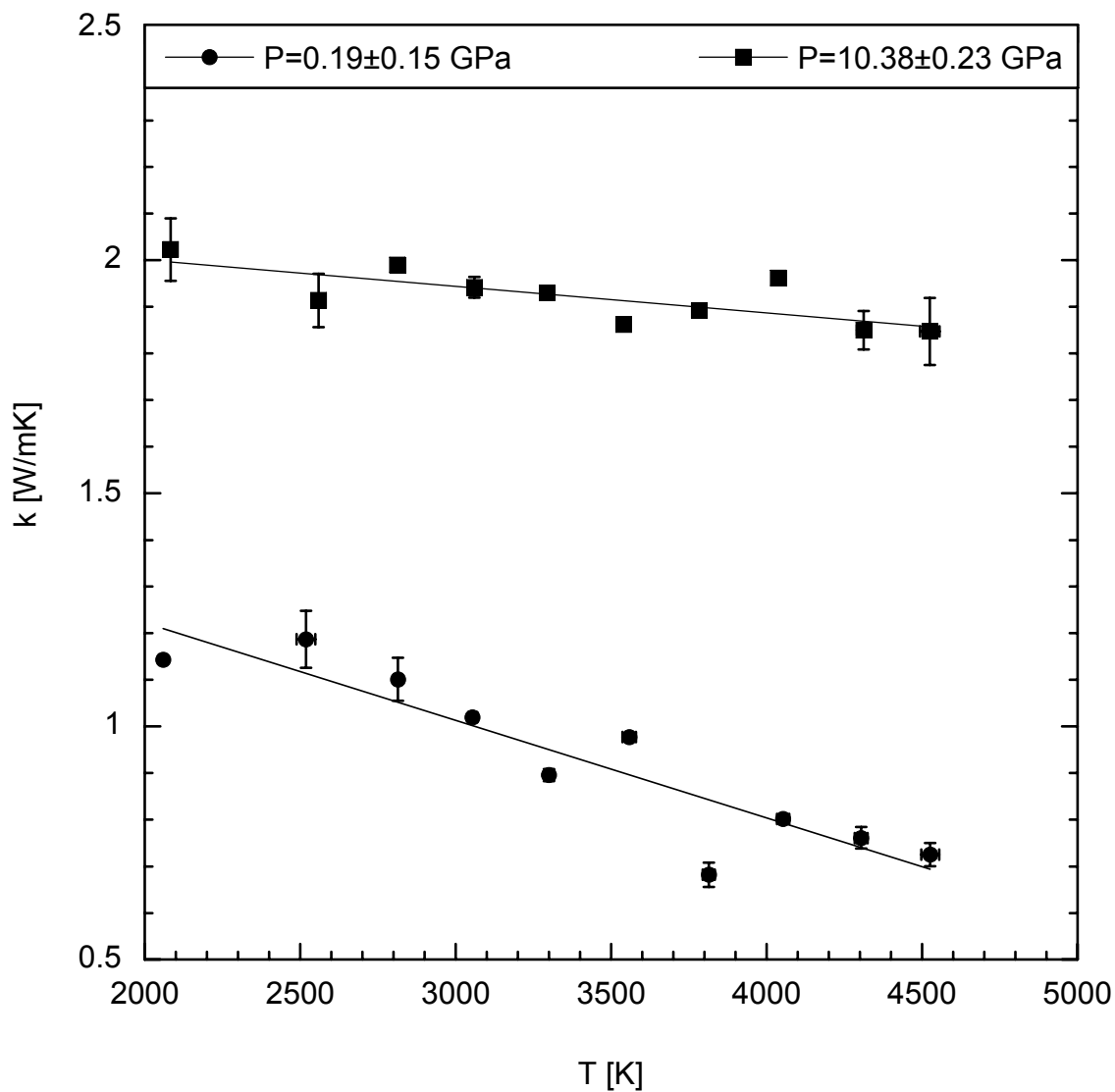
830

831

832

Revision 2

833 **Figure 4**



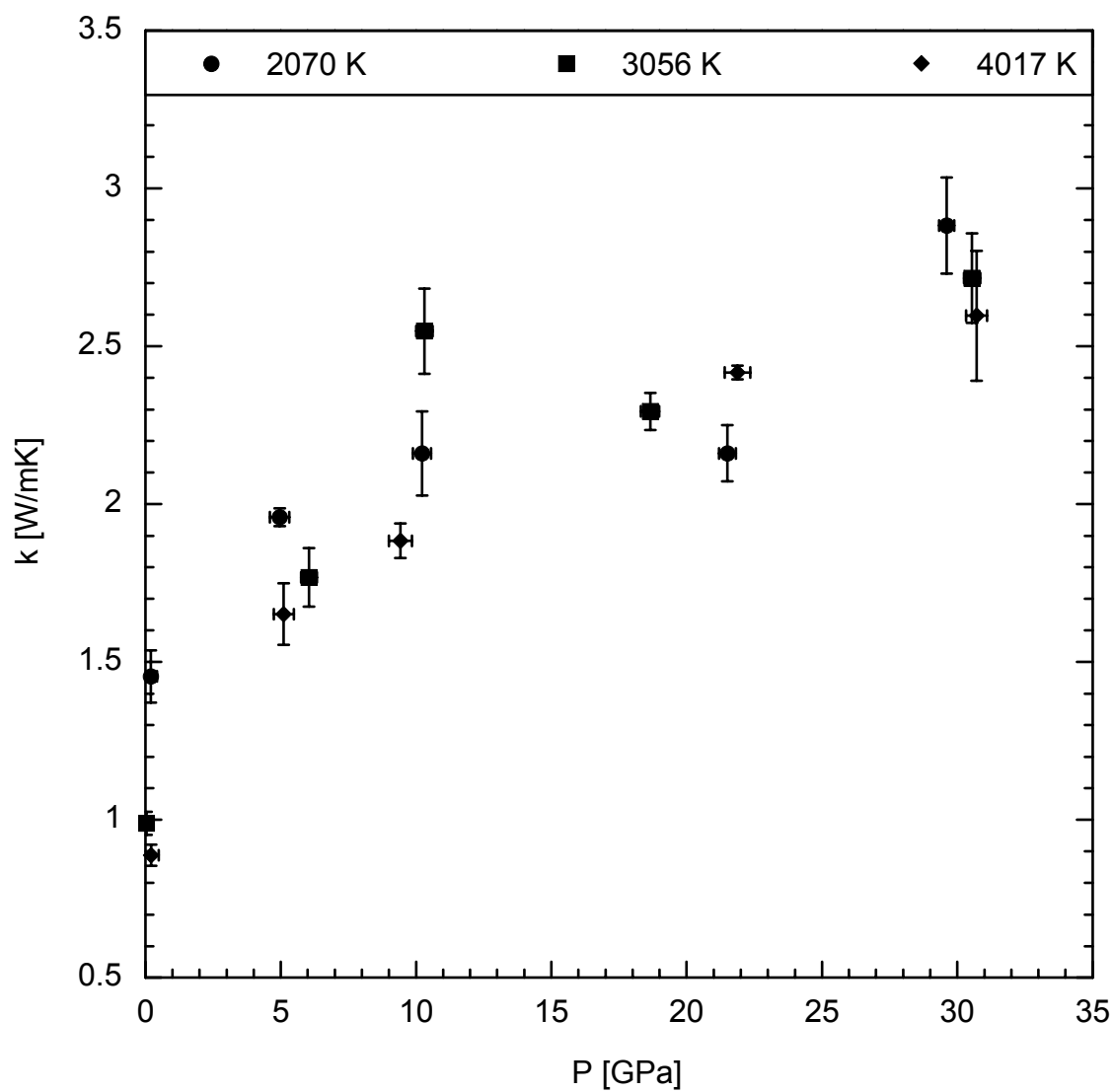
834

835

836

Revision 2

837 **Figure 5**



838

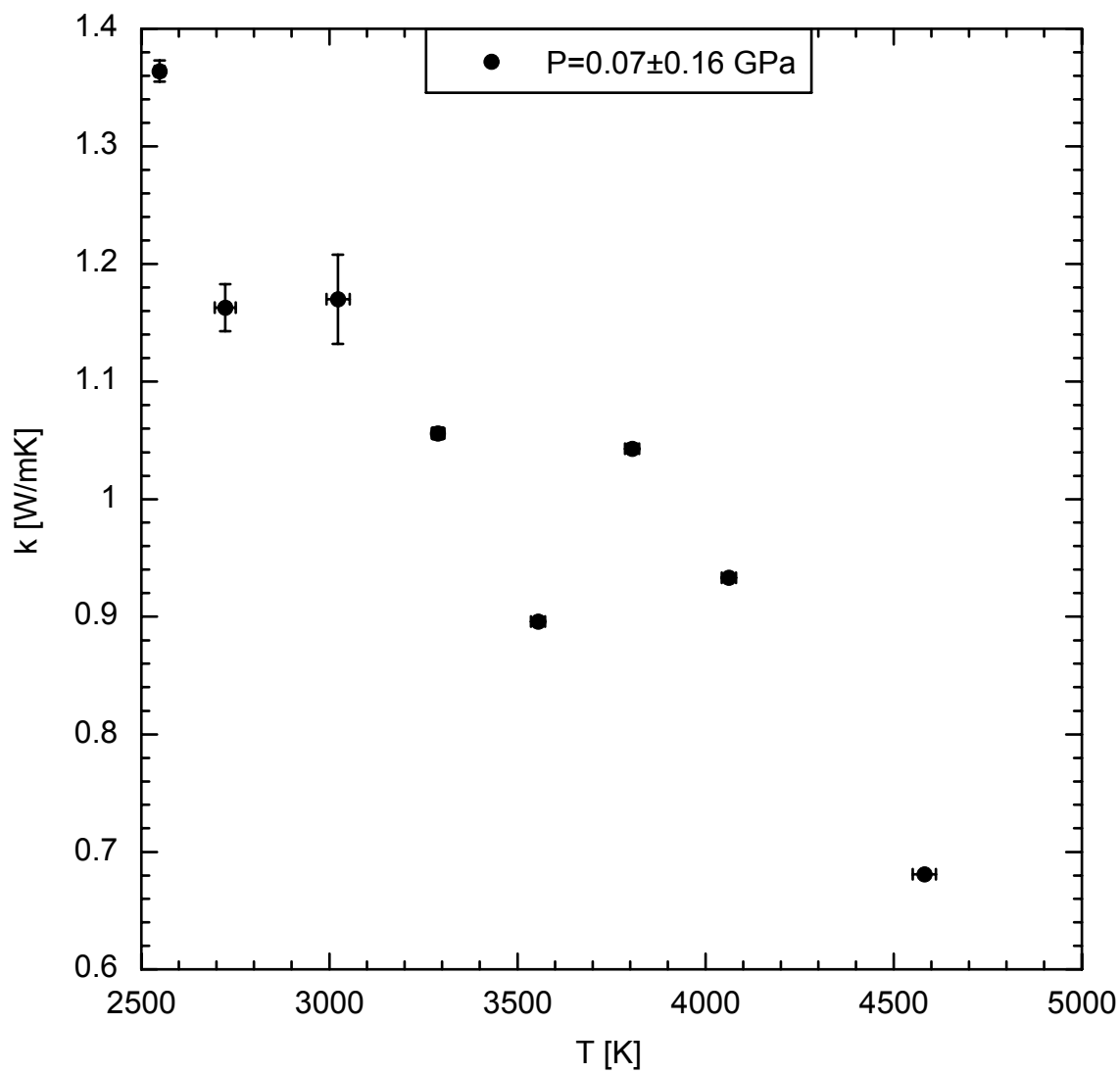
839

840

841

Revision 2

842 **Figure 6**

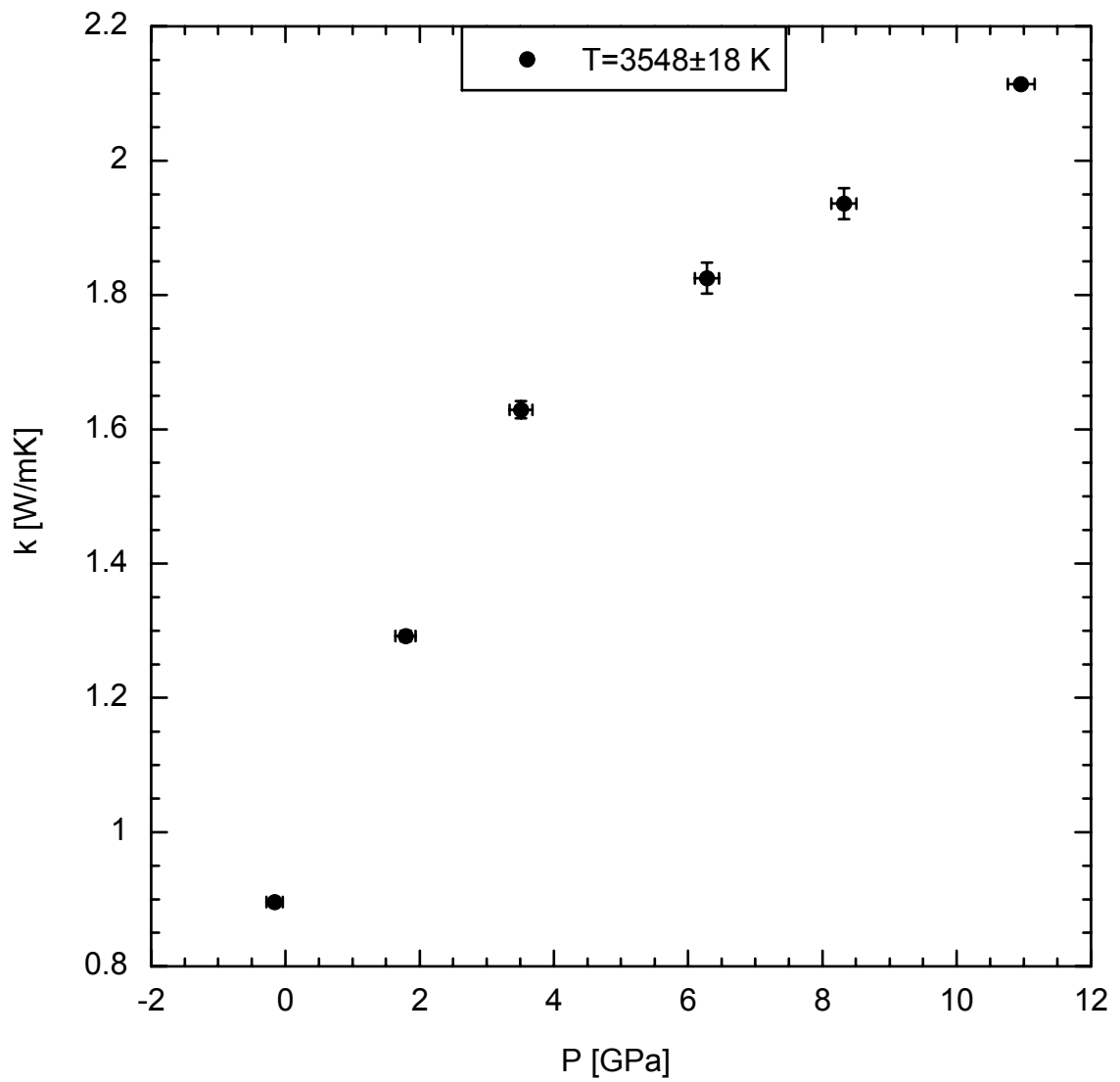


843

844

Revision 2

845 **Figure 7**



846

847